DYNAMIC FLUID-STRUCTURE ANALYSIS OF SHELLS USING THE PISCES 2 DELK COMPUTER CODE

M. S. COWLER, S. L. HANCOCK

Physics International Company, San Leandro, California 94577, U.S.A.

SUMMARY

Physics International's PISCES 2DELK computer program utilizes modern finite difference techniques to solve complex problems involving fluid-structure interaction. The most powerful feature of the PISCES 2DELK code is its ability to apply the most accurate and efficient numerical schemes to different regimes of a given problem and then couple them together in space and time. Until recently the principal numerical processors available in the code were (i) an Euler processor for the description of fluids and large distortion solid behavior, and (ii) a Lagrange processor for the description of solid continua and structures. For many engineering problems it is necessary to calculate the deformation of relatively thin shell structures. Since the stability criterion for the Lagrange processor does not allow cost efficient calculations of thin structures, a third processor has recently been added to the PISCES 2DELK library specifically for the calculation of thin shells. This paper describes the theory and capabilities of the shell processor.

The finite difference equations used in the shell processor apply to shells of arbitrary shape in either axial or translational symmetry and include full bending theory. The equations are solved explicitly and have a stability time step governed by the length of the shell segments. Prescribed loading conditions can be applied directly to a shell subgrid or they may be obtained from the interaction of the shell subgrid with one or more Euler or Lagrange subgrids. Additional boundary conditions include a semi-rigid joint model which allows the inclusion of the effects of transmission of bending moments at the junction of a number of shells without concern about the detailed stress distribution at the joint.

PISCES 2DELK code predictions are compared with experimental data from a flexible vessel test carried out at the Stanford Research Institute. Pressure and impulse correlations are presented at a number of gauge stations and the final deformations of the outer shell structure are compared. Application of PISCES 2DELK to a full HCDA involving analysis of complex shell structures is presented in a complementary paper (E5/1).

1. INTRODUCTION

Physics International's PISCES 2DELK computer program utilizes modern finite difference techniques to solve complex problems involving fluid-structure interaction. Neither a Lagrangian nor an Eulerian coordinate system is well suited to handle the entire fluid-structure interaction problem. A Lagrangian coordinate system, in which the coordinates move with the material, can accurately follow material interfaces and record the history of a piece of material for use in complex constitutive models, but a Lagrangian coordinate system fails in fluid regions where distortions are so great that coordinate tangling occurs. An Eulerian coordinate system, which remains fixed in space, can be used to calculate violent fluid flow and flow around irregular objects, but it cannot follow material interfaces as accurately as a Lagrangian coordinate system. The most powerful feature of the PISCES 2DELK code is its ability to apply the most accurate and efficient numerical schemes to the different regimes of a given problem and then couple them together in space and time.

Until recently the principal processors available in the code were a Lagrange continuum processor and an Euler continuum processor. Detailed descriptions of these processors have been given by Hancock [1]. Although these continuum processors are capable of treating the general fluid-structure interaction problem, calculations become uneconomical if relatively thin shell structures are present which restrict the stability time step required for the explicit formulations.

In order to overcome this problem a shell processor has recently been added to the PISCES 2DELK library which eliminates the dependence of the maximum stable time step on the shell thickness by imposing restrictions on the displacement field of the shell.

The following section describes the mathematical formulation used in the shell processor while section 3 outlines the technique used to couple subgrids using different types of processors. The results of a calculation are compared with experimental data in section 4.

2. MATHEMATICAL FORMULATION OF THE SHELL PROCESSOR

The explicit formulation used in the shell processor applies to shells of arbitrary shape in either axial or translational symmetry. For brevity, only the more general case of axial symmetry is described for which the curvilinear coordinate system (s, φ, θ) shown in figure 1 is used extensively.

2.1 Strain-Displacement Relations

The strain-displacement relations are derived by imposing two constraints on the displacement field, namely that (1) linear elements which are normal to the middle surface before deformation remain straight and normal to the deformed middle surface, and (2) the density of the shell remains constant (i.e., there is no volume change). The second assumption allows for significant changes in the shell thickness during plastic deformation. With these

constraints the increments in principal strains $d\varepsilon_\varphi$ and $d\varepsilon_\theta$ at a distance z from the middle surface ($-h/2 < z < h/2$) are given to first order in the shell thickness, h, by the expressions

$$d\varepsilon_\varphi = \overline{d\varepsilon}_\varphi - z\,\overline{d\chi}_\varphi \qquad d\varepsilon_\theta = \overline{d\varepsilon}_\theta - z\,\overline{d\chi}_\theta \tag{1}$$

The principal strain increments $\overline{d\varepsilon}_\varphi$ and $\overline{d\varepsilon}_\theta$ and curvatures $\overline{\chi}_\varphi$ and $\overline{\chi}_\theta$ of the middle surface are given by:

$$\overline{d\varepsilon}_\varphi = \frac{d(\Delta s)}{\Delta s} \qquad \overline{\chi}_\varphi = \frac{\Delta\varphi}{\Delta s}$$

$$\overline{d\varepsilon}_\theta = \frac{dy}{y} \qquad \overline{\chi}_\theta = \sin\varphi/y \tag{2}$$

where Δs and $\Delta\varphi$ refer to the length and subtended angle of an element on the middle surface (see figure 1). The d denotes time increments.

2.2 Stress-Strain Relations

The constitutive relations are formulated on the assumption that the stress component normal to the shell is small and can be neglected. Then a biaxial state of stress exists with the principal directions along the curvilinear coordinates of the middle surface. With this assumption large inelastic deformations are analyzed by material constitutive relations based on the incremental theory of plasticity, using the von Mises yield condition and the associated flow rule developed from the Reuss assumptions.

For a biaxial stress condition the von Mises yield function reduces to

$$f(T_{\varphi\varphi}, T_{\theta\theta}) = T_{\varphi\varphi}^2 - T_{\varphi\varphi}T_{\theta\theta} + T_{\theta\theta}^2 - \sigma_y^2 \tag{3}$$

where σ_y is the yield stress in uniaxial tension, and $T_{\varphi\varphi}$ and $T_{\theta\theta}$ are the two nonvanishing principal stress components. Elastic stress increments are obtained using Hooke's law:

$$dT_{\varphi\varphi} = \frac{E}{1-\nu^2}\left[d\varepsilon_{\varphi\varphi} + \nu d\varepsilon_{\theta\theta}\right] \qquad dT_{\theta\theta} = \frac{E}{1-\nu^2}\left[d\varepsilon_{\theta\theta} + \nu d\varepsilon_{\varphi\varphi}\right] \tag{4}$$

where E and ν are Young's modulus and Poisson's ratio respectively.

If the incremented stresses violate the yield conditions then the stresses are recalculated by decomposing the strain increments into elastic and plastic increments:

$$d\varepsilon_{\varphi\varphi} = d\varepsilon^e_{\varphi\varphi} + d\varepsilon^p_{\varphi\varphi} \qquad d\varepsilon_{\theta\theta} = d\varepsilon^e_{\theta\theta} + d\varepsilon^p_{\theta\theta} \tag{5}$$

The elastic increments must satisfy equation (4) while the plastic increments are obtained from the theory of plastic potential:

$$d\varepsilon^p_{\varphi\varphi} = \lambda\frac{\partial f}{\partial T_{\varphi\varphi}} = \lambda(2T_{\varphi\varphi} - T_{\theta\theta}) \qquad d\varepsilon^p_{\theta\theta} = \lambda\frac{\partial f}{\partial T_{\theta\theta}} = \lambda(2T_{\theta\theta} - T_{\varphi\varphi}) \tag{6}$$

where λ is a constant of proportionality.

Equations (3) to (6) are solved simultaneously to obtain the new stresses $T_{\varphi\varphi}$, $T_{\theta\theta}$. The yield stress, σ_y, may be varied to allow for post yield work hardening using either an isotropic hardening model or the mechanical sub-layer model (Hunsaker [2]).

2.3 Equations of Motion

The equations of motion for a thin axisymmetric shell are

$$m\ddot{x} = f_{xs} + f_{xe} \qquad\qquad m\ddot{y} = f_{ys} + f_{ye} \tag{7}$$

where m is the mass per unit length; $(\ddot{x},\ddot{y})$ is the acceleration; (f_{xs},f_{ys}) is the internal force per unit area; and, (f_{xe},f_{ye}) is the force per unit area due to external pressures (e.g., stress boundary conditions, interactive forces).

The shell internal forces are given by:

$$f_{xs} = -\frac{1}{y}\frac{d}{ds}(yA) \qquad\qquad f_{ys} = \frac{1}{y}\frac{d}{ds}(yB) - \frac{N_\theta}{y} \tag{8}$$

$$A = N_\varphi \sin\varphi - Q_\varphi \cos\varphi \qquad\qquad B = N_\varphi \cos\varphi + Q_\varphi \sin\varphi$$

where N_φ, N_θ are the stress resultants and Q_φ is the transverse shear.

Neglecting the effect of rotary inertia

$$Q_\varphi = \frac{dM_\varphi}{ds} + (M_\varphi - M_\theta)\cos\varphi/y \tag{9}$$

The shell element from which these equations are derived is shown in figure 2.

The stress resultants N_φ, N_θ and the bending moments M_φ, M_θ are obtained using the expressions

$$N_\varphi = \int_{-h/2}^{h/2} T_{\varphi\varphi}(z)\,dz \qquad\qquad N_\theta = \int_{-h/2}^{h/2} T_{\theta\theta}(z)\,dz$$

$$M_\varphi = \int_{-h/2}^{h/2} zT_{\varphi\varphi}(z)\,dz \qquad\qquad M_\theta = \int_{-h/2}^{h/2} zT_{\theta\theta}(z)\,dz \tag{10}$$

2.4 Finite Difference Formulation

The middle surface of the shell is represented by a number of vertices connected by linear segments. The centering of the dependent variables is illustrated in figure 3. Shell coordinates (x,y), velocity components $(\dot{x}, \dot{y})$, bending moments, M_φ, M_θ and the principal curvatures of the middle surface $\overline{\chi}_\varphi$, $\overline{\chi}_\theta$ are centered at vertices. Stress resultants N_φ, N_θ, the thickness, h, the angle, φ, the segment lengths Δs and the middle surface strains $\overline{\epsilon}_\varphi$, $\overline{\epsilon}_\theta$ are centered at mid-segment positions. This centering is compatible with that used in the Lagrang continuum processor and allows straightforward coupling and easy application of boundary conditions.

A calculation cycle which advances the solution from time t^n to t^{n+1} proceeds as described below.

(1) The velocity and positions of shell vertices are updated by applying Newton's law and integrating

$$m_i(\ddot{x})_i^n = (f_{xs})_i^n + (f_{xe})_i^n \qquad\qquad m_i(\ddot{y})_i^n = (f_{ys})_i^n + (f_{ye})_i^n$$

$$(\dot{x})_i^{n+\frac{1}{2}} = (\dot{x})_i^{n-\frac{1}{2}} + (\ddot{x})_i^n \Delta t^n \qquad\qquad (\dot{y})_i^{n+\frac{1}{2}} = (\dot{y})_i^{n-\frac{1}{2}} + (\ddot{y})_i^n \Delta t^n$$

$$(x)_i^{n+1} = (x)_i^n + (\dot{x})_i^{n+\frac{1}{2}}\Delta t^{n+\frac{1}{2}} \qquad (y)_i^{n+1} = (y)_i^n + (\dot{y})_i^{n+\frac{1}{2}}\Delta t^{n+\frac{1}{2}}$$

where m_i is the mass associated with the ith vertex.

(2) Strains and curvatures of the middle surface are evaluated using equation (2).

$$(\Delta s)_{i+\frac{1}{2}}^{n+\frac{1}{2}} = \sqrt{\left\{(\Delta x_{i+\frac{1}{2}})^2 + (\Delta y_{i+\frac{1}{2}})^2\right\}}$$

$$(\overline{d\varepsilon}_\varphi)_{i+\frac{1}{2}}^{n+\frac{1}{2}} = \frac{\Delta t^{n+\frac{1}{2}}}{\left[(\Delta s)_{i+\frac{1}{2}}^{n+\frac{1}{2}}\right]^2}\left(\Delta x_{i+\frac{1}{2}} \cdot \Delta\dot{x}_{i+\frac{1}{2}} + \Delta y_{i+\frac{1}{2}} \cdot \Delta\dot{y}_{i+\frac{1}{2}}\right)$$

$$(\overline{d\varepsilon}_\theta)_{i+\frac{1}{2}}^{n+\frac{1}{2}} = \Delta t^{n+\frac{1}{2}}\left\{(\dot{y})_{i+1}^{n+\frac{1}{2}} + (\dot{y})_i^{n+\frac{1}{2}}\right\}\Big/\left\{(y)_{i+1}^{n+\frac{1}{2}} + (y)_i^{n+\frac{1}{2}}\right\}$$

where $\Delta x_{i+\frac{1}{2}} = (x)_{i+1}^{n+\frac{1}{2}} - (x)_i^{n+\frac{1}{2}}$, $\Delta\dot{x}_{i+\frac{1}{2}} = (\dot{x})_{i+1}^{n+\frac{1}{2}} - (\dot{x})_i^{n+\frac{1}{2}}$

and similarly for $\Delta y_{i+\frac{1}{2}}$, $\Delta\dot{y}_{i+\frac{1}{2}}$.

The meridional curvature $(\overline{\chi}_\varphi)_i^{n+1}$ is evaluated by constructing a circle with center $\left((x_c)_i^{n+1}, (y_c)_i^{n+1}\right)$ through the vertices i-1, i, and i+1. The hoop curvature $(\overline{\chi}_\theta)_i^{n+1}$ is then obtained from the relation

$$(\overline{\chi}_\theta)_i^{n+1} = \frac{(y)_i^{n+1} - (y_c)_i^{n+1}}{(y)_i^{n+1}} \cdot (\overline{\chi}_\varphi)_i^{n+1}$$

(3) The stress resultants $(N_\varphi)_{i+\frac{1}{2}}^{n+1}$, $(N_\theta)_{i+\frac{1}{2}}^{n+1}$ and bending moments $(M_\varphi)_i^{n+1}$, $(M_\theta)_i^{n+1}$ are obtained by performing the integration in equation (10). Using equations (3) to (6) the stresses $T_{\varphi\varphi}^{n+1}$, $T_{\theta\theta}^{n+1}$ are evaluated at a number of Gaussian integration stations through the shell thickness and Gaussian quadrature is used to obtain the required integrals.

(4) The force assigned to a shell node due to internal shell stresses is equal to the summation of contributions from all adjoining shell segments. There are two adjoining segments at a regular node, one at an end point, and several at a multi-shell branch point. The force equations are derived by an integration method similar to the one described in reference [3]for Lagrange quadrilateral zones. For a shell segment running from node i to node i+1, the forces are calculated as follows (all quantities are centered at time level n+1):

$$(f_{xs})_{i+1} = \pi A\left[2y_{i+\frac{1}{2}} - \Delta s_{i+\frac{1}{2}}\cos\varphi\,(y_{i+\frac{1}{2}} - y_{i+1})/y_{i+\frac{1}{2}}\right]$$

$$(f_{xs})_i = -(f_{xs})_{i+1}$$

$$(f_{ys})_{i+1} = -\pi y_{i+1}(2B-C)$$

$$(f_{ys})_i = \pi y_i(2B+C)$$

where $A = (N_\varphi \sin_\varphi - Q_\varphi \cos_\varphi)_{i+\frac{1}{2}}$ $\qquad B = (N_\varphi \cos\varphi + Q_\varphi \sin\varphi)_{i+\frac{1}{2}}$

$C = \left[\Delta s(B\cos\varphi - N_\theta)/y\right]_{i+\frac{1}{2}}$

$\sin\varphi = (x_i - x_{i+1})/\Delta s_{i+\frac{1}{2}}$ $\qquad \cos\varphi = (y_{i+1} - y_i)/\Delta s_{i+\frac{1}{2}}$

and $Q_\varphi = (M_{\varphi\ i+1} - M_{\varphi\ i})/\Delta s_{i+\frac{1}{2}} + \frac{1}{2}\cos\varphi\left[\alpha_i(M_\varphi - M_\theta)_i + \alpha_{i+1}(M_\varphi - M_\theta)_{i+1}\right]$

with $\alpha_i = 0$ if $y_i = 0$, $\alpha_i = 1/y_i$ otherwise, and similarly for α_{i+1}.

The terms A, B, C, $\sin\varphi$, $\cos\varphi$, and Q are all centered at $i+\frac{1}{2}$.

The mass contributed to nodes i and i+1 is one half of the mass of revolution of the shell segment.

(5) If an external pressure, p, acts on a shell segment, the force exerted on the segment is

$$(f_{xe})_{i+\frac{1}{2}} = 2\pi y_{i+\frac{1}{2}}(y_{i+1} - y_i)p \qquad (f_{ye})_{i+\frac{1}{2}} = 2\pi y_{i+\frac{1}{2}}(x_i - x_{i+1})p$$

This assumes that the pressure is on the left as we travel from node i to node i+1; opposite signs are used for a pressure load on the other side of the shell. This segment load is distributed to nodes i and i+1 using

$$(f_{xe})_i = (f_{xe})_{i+1} = \frac{1}{2}(f_{xe})_{i+\frac{1}{2}} \qquad (f_{ye})_i = \frac{1}{2}(f_{ye})_{i+\frac{1}{2}}\, y_i/y_{i+\frac{1}{2}}$$

$$(f_{ye})_{i+1} = (f_{ye})_{i+\frac{1}{2}} - (f_{ye})_i$$

3. INTERFACE CALCULATIONS

The force-mass method used to calculate the acceleration of vertices of shell subgrids makes it very simple to join different Lagrange and shell subgrids together. The total force associated with an interactive vertex (a vertex belonging to more than one subgrid) is simply the sum of the forces exerted on it by all surrounding zones/segments of each subgrid. The mass associated with the vertex is the sum of the masses contributed by each of the surrounding zones/segments of each subgrid. Forces exerted by Euler subgrids are included in the above summations, but no mass contributions are made by Euler subgrids. Thus Euler subgrids provide a pressure boundary condition for Lagrange or shell subgrids. In return Lagrange or shell subgrids present geometric obstacles to the flow of material in Euler subgrids.

The Euler cells adjacent to a Lagrange or shell interface generally have irregular shapes. Their volumes and face areas change during the calculation as the Lagrange or shell mesh moves across the Euler mesh. Euler cells which are initially covered by the Lagrange or shell subgrids may become uncovered during the calculation and fill with fluid while uncovered cells may become covered. The most complicated aspect of the Euler-Lagrange, Euler-shell coupling calculation is the process called blending. If an interface Euler cell has a large face area-to-volume ratio, as compared to a noninterface cell, its natural time step for stability becomes very small. If computed independently, such an interface cell would control the time step for the entire calculation, and this controlling time step would approach zero as the cell became covered. The solution to this problem is to combine (blend) such a small cell with a large neighbor to form a single larger cell. Up to four small cells can be blended together in PISCES 2DELK. The blending process is activated automatically when needed and conserves mass, momentum, and energy.

A semi-rigid joint model can be used to join several Lagrange or shell subgrids together. This model allows one to include the effects of transmission of bending moments at the junction without concern as to the detailed stress distribution at the joint. The model consists of the kinematic constraint that vertices surrounding a joint all rotate at the same angular velocity about the joint. This is equivalent to assuming that the angle between any two radial vertices remains constant.

4. TEST CALCULATION

Test data are available from a number of flexible vessel experiments performed by the Stanford Research Institute [4]. The experiments were designed to simulate a hypothetical core disruptive accident (HCDA) in a scaled reactor vessel. PISCES 2DELK calculations have been performed on three of the SRI experiments as part of the APRICOT (Analysis of PRImary COntainment Transients) program, a U. S. Department of Energy-sponsored project to verify the capabilities of large computer codes to analyze HCDA. A portion of the results from one of these calculations (FV102) is presented here. Detailed results of all three calculations are given elsewhere (Cowler and Hancock [5]).

The experimental and calculational geometries for the results described here are compared in figure 4. The experiment consisted of a flexible vessel containing a flexible core barrel with a low density explosive energy source inside to simulate a HCDA load. The vessel was filled nearly to the top with water. A Mylar diaphragm was clamped across the core barrel to prevent water from entering the area of the energy source. Pressure transducers were mounted in the locations indicated in figure 4(a).

For the finite difference representation (figure 4(b)) a single Euler subgrid was used to model the energy source, water, and air gap. Shell subgrids were used to model the NI-200 outer vessel and the aluminum shell surrounding the core barrel. The aluminum shell was joined along its entire length to a Lagrange subgrid which modelled the lead core barrel. Material data and the pressure-volume relation for the energy source were taken from reference [4].

Calculated and experimental pressure and impulse records at a gauge location on the outer wall, floor, and roof of the vessel are compared in figure 5. In general the calculated pressures agree well with the experimental data. At late times some numerical oscillations can be observed at gauge stations 4 and 5. These oscillations arise because the present explicit solution procedure is unable to deal adequately with the effects of fluid cavitation. Nevertheless the impulses at these locations are in good agreement with the experiment.

At gauge station 8, on the roof of the vessel, the pressure pulse generated by the initial impact of the water on the roof is predicted well in time, amplitude, and duration. The second pulse at 1.2 ms is predicted well in

amplitude but not in time. The calculation shows that this pulse is caused by a second impact of the water after being separated from the roof immediately following the initial impact. This second impact is produced by the first wave, generated during the initial impact, being reflected at the vessel wall. The velocity at which this wave travels depends critically on the curvature of the fluid surface at the time of initial impact and it is thought that a small error in the calculated curvature probably caused the time delay of the second pulse observed in the calculation.

The final displacement of the containment vessel is compared with the experimental profile in figure 6. The overall agreement is very good. At the top of the vessel the calculation slightly overestimates the displacement while in the lower region the trend is reversed.

References

[1] S. L. Hancock, "Finite Difference Equations for PISCES 2DELK, A Coupled Euler-Lagrange Continuum Mechanics Computer Program." Physics International Co. Technical Memorandum TCAM 76-2 (1976).

[2] B. Hunsaker et al, "A Comparison of Current Work-Hardening Models Used in the Analysis of Plastic Deformations." TEES 2926-73-3, Aerospace Engineering Dept. Texas A&M University (1973).

[3] S. L. Hancock, "Equations for Forces in Axisymmetric Lagrange Zones." 2nd International Conference on Numerical Methods in Nonlinear Mechanics, University of Texas at Austin, March (1979).

[4] D. J. Cagliostro et al, "Experiments on Response of Rigid and Flexible Reactor Vessel Models to a Simulated HCDA." SRI Contract 31-109-98-2655, (1976).

[5] M. S. Cowler, S. L. Hancock, "PISCES 2DELK Calculations on APRICOT Problems 5, 6, and 7." Physics International Co. Technical Memorandum, TCAM 78-1 (1978).

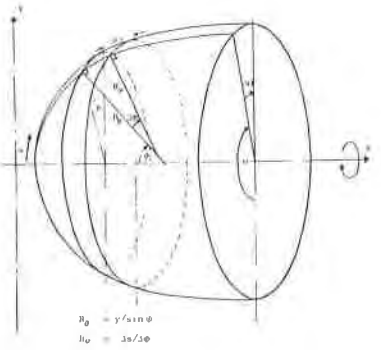

Figure 1: Coordinate Systems for a Shell of Revolution

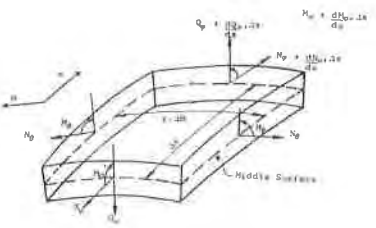

Figure 2: Element of a Shell of Revolution

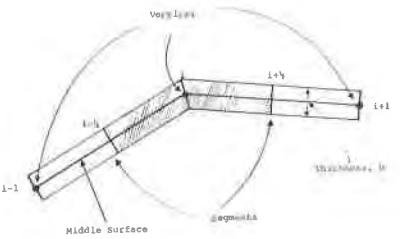

Figure 3: Finite Difference Representation of a Shell

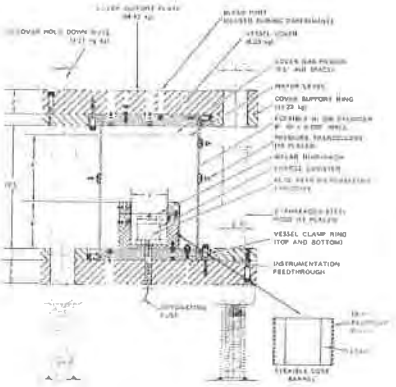

Figure 4(a): Experimental Geometry for Experiment FV102

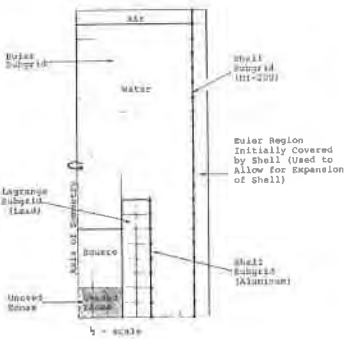

Figure 4(b): Calculation Geometry for Experiment FV102

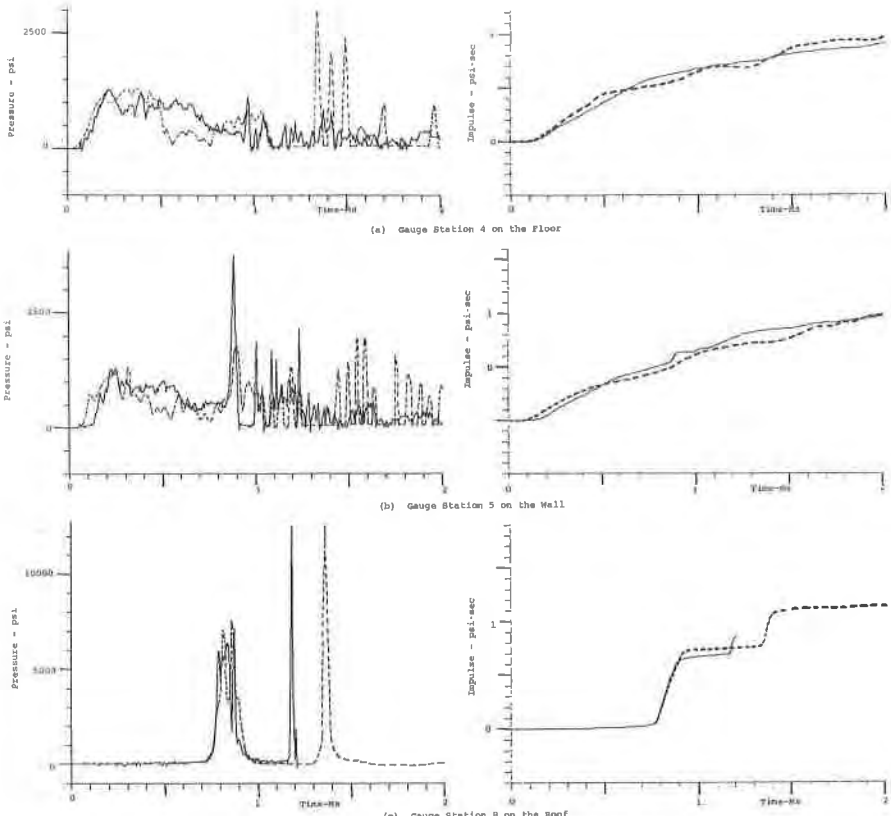

Figure 5: Pressure and Impulse Histories at Three Gauge Stations in Experiment FV102.

Figure 6: Final Displacement of the Containment Vessel in Experiment FV102.